Calibration of the Geostationary Imaging Fourier Transform Spectrometer (GIFTS)

F. A. Best[a], H. E. Revercomb[a], G. E. Bingham[b], R. O. Knuteson[a],
D. C. Tobin[a], D. D. LaPorte[a], and W. L. Smith[c]

[a]University of Wisconsin-Madison, Madison, WI
[b]Utah State University, Logan, UT
[c]NASA Langley Research Center, Hampton, VA

ABSTRACT

The NASA New Millennium Program's Geostationary Imaging Fourier Transform Spectrometer (GIFTS) requires highly accurate radiometric and spectral calibration in order to carry out its mission to provide water vapor, wind, temperature, and trace gas profiling from geostationary orbit. A calibration concept has been developed for the GIFTS Phase A instrument design. The in-flight calibration is performed using views of two on-board blackbody sources along with cold space. A radiometric calibration uncertainty analysis has been developed and used to show that the expected performance for GIFTS exceeds its top level requirement to measure brightness temperature to better than 1 K. For the Phase A GIFTS design, the spectral calibration is established by the highly stable diode laser used as the reference for interferogram sampling, and verified with comparisons to atmospheric calculations.

Keywords: Imaging, FTS (Fourier Transform Spectrometer), Spectrometer, Calibration, Remote sensing

1. INTRODUCTION

As the third in a series of earth orbiting missions, the NASA New Millennium Program has selected the GIFTS mission, which will fly an Imaging Fourier Transform Spectrometer (FTS) to provide enormous advances in water vapor, wind, temperature, and trace gas profiling from geostationary orbit[1,2]. Imaging FTS offers an instrument approach that can satisfy the demanding radiometric and spectral accuracy requirements for remote sensing and climate applications, while providing the massively parallel spatial sampling needed for rapid high spatial resolution coverage of the whole globe, as well as frequent coverage of selected regions. The top-level calibration requirement is to measure brightness temperature to better than 1 K, with a reproducibility of ±0.2 K. A calibration concept has been developed for the GIFTS instrument configuration defined in the Phase A study. For in-flight radiometric calibration, GIFTS uses views of two on-board blackbody sources (300 K and 265 K) along with cold space sequenced at regular, programmable intervals. The difference between the two internal blackbody views provides the sensor slope term in the calibration equation, while the deep space view corrects for radiant emission from the telescope by establishing the offset term. The blackbody references are cavities that follow the University of Wisconsin (UW) Atmospheric Emitted Radiance Interferometer (AERI) design[3,4,5], scaled to the GIFTS beam size.

This paper presents the general radiometric calibration approach for the Phase A GIFTS instrument design along with the expected performance. The GIFTS spectral calibration approach will also be described. This calibration is established by the highly stable diode laser used as the reference for interferogram sampling (the GIFTS Phase A Baseline laser stability is 1 in 10^6) and verified with comparison to atmospheric calculations. As the GIFTS instrument design matures some of the calibration concepts may change to match the eventual hardware configuration. This paper deals only with on-orbit calibration. An extensive program for ground calibration and testing is currently being planned.

2. RADIOMETRIC CALIBRATION

2.1 Background

The GIFTS Phase A design follows the general approach used or planned for other atmospheric sounding instruments for which high absolute accuracy is needed. For radiometric calibration, GIFTS will periodically view one or more accurately characterized blackbody references and cold space during scheduled calibration sequences. The basic techniques needed for a state-of-the-art interferometer are the same as those needed for a more conventional radiometer (e.g. current NOAA

sounders), and in fact, these same techniques yield more accurate results for an interferometer because of the lack of the uncertainties associated with broadband spectral channels[6]. Noise in the IR signal is considered separately from calibration errors. We expect the noise to be limited by detector noise (the interferometrically generated noise will be less than photon and thermally generated random noise). Recent enhanced emphasis on calibration accuracy for ground-based (UW AERI instruments for DOE climate/radiative transfer work and the Planetary Imaging FTS Lab Instrument[8]), airborne (UW HIS and Scanning HIS sounders; LaRC/MIT Lincoln Labs/UW NAST[9]; Harvard INTESA), and spacecraft FTS instruments (SDL CIRRUS 1A[10]; NPOESS CrIS interferometer design and demonstration units) will be reflected in the procedures used for this program.

There are two options for the GIFTS radiometric calibration implementation that allow different spacecraft interface constraints to be addressed. One follows the traditional approach of using a large area external blackbody viewed with a flat pointing mirror that is also used to view cold space and the earth (e.g. the current GOES imager and sounder or the GHIS Phase B design). The second option replaces the large area external blackbody with a pair of internal small cavity blackbodies at different temperatures. There is a precedent for the use of a single blackbody approach in the Visible Infrared Spin-scan Radiometer Atmospheric Sounder (VAS)[11]. Here we mainly discuss the internal blackbody approach, but the overall performance of both systems is compared and shown to meet advanced sounding requirements.

2.2 Internal Blackbodies

Radiometric calibration for the GIFTS Phase A instrument design is achieved by two small aperture internal reference blackbodies, viewed by a small 45° turning mirror located close to the telescope field image. The blackbody design is a scaled version (linear dimensions reduced by a factor of 2.7) of the current UW AERI blackbodies and consist of a cone, cylinder, and inverted partial cone with an aperture of 2.5 cm (see Figure 1).

The cavity surface for the GIFTS blackbodies will most likely be Chemglaze Z306, as used for the AERI blackbodies, although a specular surface will also be considered. With Chemglaze Z306, the cavity spectral emissivity ranges between 0.993 and 0.996 with an absolute uncertainty of < 0.002. The cavity is supported structurally and isolated thermally from the case by the Cavity Structural Support. Radiative coupling between the cavity and case is minimized by the use of multi-layer insulation. Each cavity has a redundant set of four YSI Super-stable thermistors that are used for both temperature measurement (fully characterizing the cavity gradients), and temperature control. Heater wire wound around the cavity allows each reference blackbody to be run at or above ambient temperature. For GIFTS, one blackbody will be temperature controlled to about 300 K and

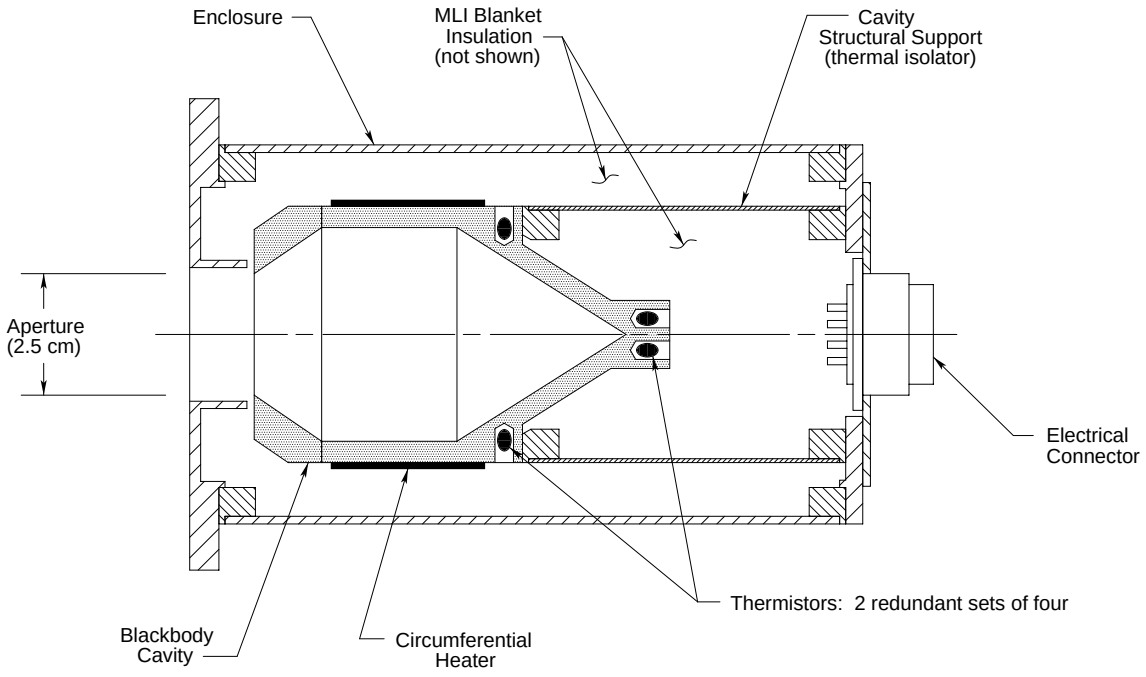

Figure 1. GIFTS Internal Blackbody crossectional view. This design follows from the UW-developed AERI blackbody, with a reduction in physical size by a factor of 2.7.

the other will be thermally coupled to the telescope structure expected to run at 265 K. The GIFTS blackbody temperature uncertainties are expected to be ~0.07 K (the AERI blackbody performance has been demonstrated by comparison with a NIST maintained blackbody reference showing agreement to better than 0.05 K for temperatures from 293 to 333 K[12,13]).

Currently, Monte Carlo ray trace analysis is being conducted to help characterize the spatial distribution of radiance at the aperture of the cavity. This analysis includes both surface paint reflectivity characteristics and cavity temperature gradients. The ray trace analysis is also being used to bound the uncertainty in cavity radiance resulting from specified uncertainties and distributions of surface emissivity.

2.3 Radiometric Calibration Uncertainty Analysis

This section describes the relationships that are used to determine the GIFTS radiometric calibration uncertainty. Assume that we represent the complex, uncalibrated spectrum for incident radiance N by

$$C = \left[N\tau_t + B_t \left(1-\tau_t\right)\right] R_f + C_f \tag{1}$$

where τ_t is the transmission of the telescope (and external pointing mirror, if included), B_t is the Planck emission at the temperature of the telescope, R_f is the complex responsivity of the portion of the instrument behind the telescope, and C_f is the complex offset arising from the same portion of the instrument behind the telescope. The term in the square brackets is the radiance incident on the turning flat, assuming there is no scattering from the telescope mirror. Similarly, the uncalibrated spectra for the internal hot and cold blackbodies can be represented as

$$C_H = B_H R_f \ + \ C_f \text{ and } C_C \ = \ B_C R_f + C_f \tag{2}$$

where the radiance emitted by the blackbodies is represented by B_H and B_C. Differencing the equations in 2 shows that the complex responsivity is given by

$$R_f \ = \ \frac{C_H - C_C}{B_H - B_C} \tag{3}$$

Therefore, the responsivity excluding the telescope can be monitored without changing the instrument pointing. Careful control of the detector temperature and use of low temperature-coefficient electronics should make the responsivity a very stable quantity.

Now, since the space view raw spectrum is given by Equation 1 with the scene radiance N replaced by B_s (which consists of space emission and any warmer tail of the field of view), differencing an earth view C_E and a space view C_S spectra removes the instrument background contribution and yields the relationship

$$N \ = \ \frac{1}{\tau_t} Re\left(\frac{C_E \ - C_S}{R_f} \right) \ + B_s \ = \ \frac{1}{\tau_t} \ (B_H - B_C) Re\left(\frac{C_E \ - C_S}{C_H - C_C} \right) + B_s \tag{4}$$

where Equation 3 has been used to eliminate the complex responsivity and where *Re* stands for the real part of the complex spectral ratio. The subtraction of the background assumes that instrument emissions have not changed significantly between the space view and the earth view. In practice, the space views must be performed frequently enough that temporal interpolation can approximate the required simultaneity with only small errors.

If the telescope transmission were known, Equation 4 would be the basic calibration relationship. In fact, the transmission will be measured both from piece-part reflectivity measurements and from full aperture blackbody observations on the ground, so it will be well known at the start of the mission. The equation is very similar to that for a full aperture "hot" blackbody calibration approach for which the cold blackbody raw spectrum in the denominator would be replaced by the space view spectrum C_S .

However, we do not need to rely on the stability of the telescope transmission in flight. The transmission will be determined by differencing the space and the cold blackbody views and using the measured temperature of the telescope optical elements.

$$C_S - C_C \;=\; \left[(1-\tau_t)B_t + \tau_t B_s \;-\; B_C\right] R_f \tag{5}$$

Solving for the transmission and using Equation 3 to eliminate the responsivity yields

$$\tau_t = 1 - \frac{1}{B_t} Re\left(B_C + \frac{C_S - C_C}{R_f} \right) = \frac{B_t - Re\left(B_C + \frac{C_S - C_C}{R_f} \right)}{B_t - B_s}$$

$$= 1 - \frac{1}{B_t}\left[B_C + (B_H - B_C) Re\left(\frac{C_S - C_C}{C_H - C_C} \right) \right] = \frac{B_t - B_c - \left(B_H - B_C\right) Re\left(\frac{C_S - C_C}{C_H - C_C} \right)}{B_t - B_s} \tag{6}$$

It should only be necessary to perform this observation very infrequently, but the cold view should be performed close in time to the space view to make sure that the instrument backgrounds accurately cancel. Note that for a high transmission, the temperature of the optical elements (or the effective emitting temperature associated with the non-unity transmission of the telescope) does not need to be known very accurately to reduce uncertainties arising from the transmission determination to very low levels.

Note that in both Equations 4 and 6, the ratio of differences of complex spectra automatically eliminates the phase of the raw spectra[7]. As for an external blackbody calibration, phase correction is not needed and in fact, should be avoided.

To summarize this approach, the emission from the telescope is removed by subtracting the space view from the earth view, and the responsivity (excluding the telescope transmission) is provided by the internal blackbody views. The telescope transmission is both determined prelaunch and monitored from the calibration views in flight. Both time interpolation of the space views and telescope temperature measurement are used to assure accurate subtraction of telescope emission while minimizing the required frequency of space views.

2.4 Expected Radiometric Accuracy

Figure 2 shows the GIFTS baseline calibration radiometric accuracy compared to the external blackbody approach, assuming the same parameter uncertainties for both, except for the emissivity uncertainty of the external blackbody (increased to 0.005 to account for its lower cavity enhancement factor). At each scene temperature, the calibration accuracy is the root sum square (RSS) combination of several system uncertainties, including those due to temperature and emissivity for each of the blackbodies, the structure temperatures affecting reflection from the blackbodies, and the telescope mirror reflectivity. Also included is the contribution from the time variation of the telescope temperature between the space and earth views. For the case where the transmission is known, we have assumed that ground based testing with a large external blackbody has determined the transmission of the telescope to within 0.2%. Table 1 presents the input parameters and uncertainty magnitudes that were used in the uncertainty analysis model to generate the GIFTS calibration accuracies presented in Figure 2. Figure 3 illustrates the individual error contributions at 2000 wavenumbers due to the temperature stability parameters and uncertainty magnitudes shown in Table 1. Even including the uncertainty due to the characterization of the telescope

transmission in-flight, the expected calibration accuracy is well within the nominal 1 K requirement for accurate atmospheric sounding (the short wavelengths are not used for the cold scene temperatures of the upper atmosphere).

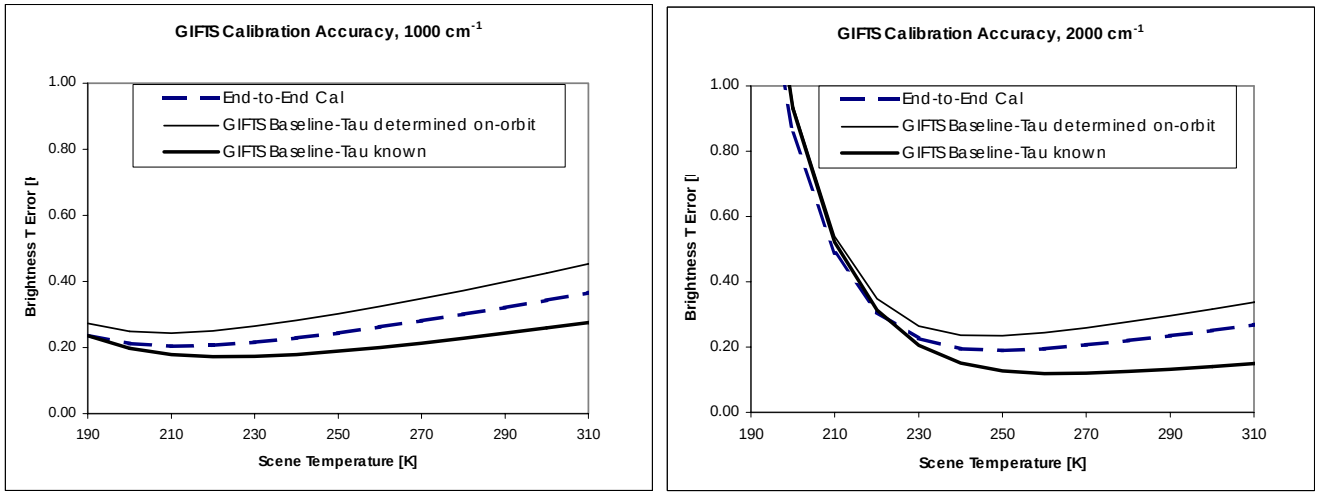

Figure 2. GIFTS calibration accuracy at wavenumbers of 1000cm^{-1} (left) and 2000 cm^{-1} (right). The three cases plotted for each wavenumber represent the baseline GIFTS Phase A design where the telescope reflectivity is known from pre-launch characterization, a worst case assumption using only on-orbit determination of telescope reflectivity, and the external large area blackbody option (labelled "End-to-End Cal".

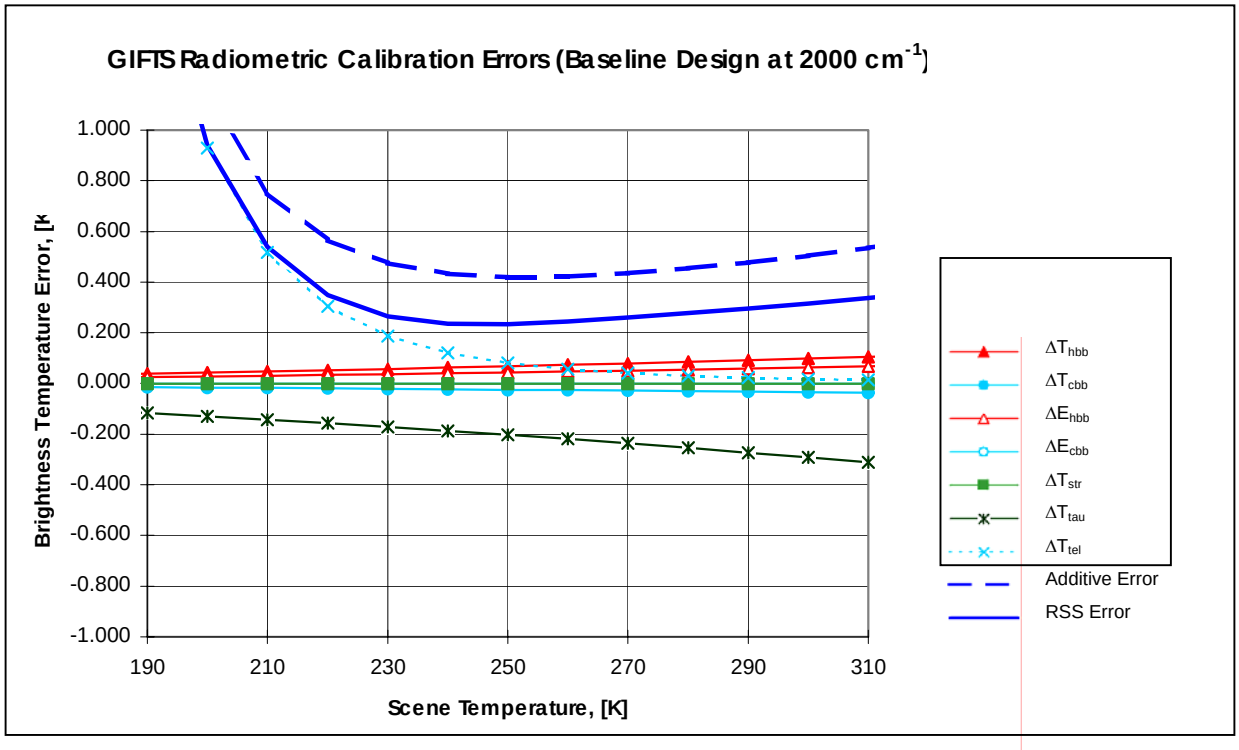

Figure 3. GIFTS radiometric calibration errors at 2000 wavenumbers by individual contributor. The additive and RSS accumulation of the errors are shown (dashed and solid line respectively). The RSS curve in this figure is plotted as "GIFTS Baseline-Tau determined on-orbit" on the right side of Figure 2.

Input Parameters		
wn	Wavenumber [cm^{-1}]	2000
tau	Telescope (2) elements and blackbody mirror transmission	0.913
Thbb	Hot blackbody temperature [K]	300
Tcbb	Cold blackbody temperature [K]	265
Tspace	Temperature of space [K]	4
Ttel	Telescope temperature [K]	265
Tstr	Temperature of structure reflecting into BB's	265
Ehbb	Emissivity of hot blackbody	0.996
Ecbb	Emissivity of cold blackbody	0.996
Parameters Used For Temperature Stability		
Etel	Telescope emissivity	0.087
TauTot	Total transmission through instrument	0.205
TtelΔ	Change in telescope temp between earth and space views [K]	0.5
Uncertainty Magnitudes		
ΔThbb	[K]	0.07
ΔTcbb	[K]	0.07
ΔEhbb	[K]	0.002
ΔEcbb	[K]	0.002
ΔTstr	[K]	5
Δtau	RSS value	0.0086
ΔTtel	[K]	2

Table 1. Calibration uncertainty analysis parameters.

3. SPECTRAL CALIBRATION

3.1 Background

The spectral calibration used for GIFTS will build upon the experience of ground-based and aircraft FTS systems (AERI, HIS, S-HIS, and NAST-I) designed with a single on-axis field-of-view (FOV). The spectral characteristics of these instruments can be defined by an Instrument Line Shape (ILS) and a spectral sampling interval. The observed spectrum is the atmospheric spectrum convolved with the ILS and sampled at equally spaced points starting at zero wavenumbers (ignoring radiometric calibration errors and noise).

The spectral sampling scale is maintained very accurately by the stable laser used to trigger sampling at equal intervals of Optical Path difference (OPD). Because the wavenumber samples are known to be equally spaced as well, the calibration of this spectral scale is determined for an entire, broad spectral band by the determination of the proper wavenumber for any single spectral feature in the band. We use the comparison of observed atmospheric spectra to line-by-line radiative transfer calculations (based on observed atmospheric state parameters) to determine the proper wavenumber scale. This calibration process transfers the very accurate positions of prominent spectral line features in the HITRAN database to the observed spectral scale. We define an effective laser wavenumber parameter to describe this scale. Once the effective laser wavenumber for a given instrument is known, interpolation techniques can be used to rigorously transform the spacing to a standard wavenumber scale allowing standardization of the spectra from different instruments. This is routinely performed for the multiple AERI instruments deployed for the US DOE Atmospheric Radiation Measurement Program.

The ILS for these existing FTS systems is determined by the maximum OPD sampled (X) and the range of field angles through the interferometer that contribute to the signal (defined by an effective half-angle, *b*, for an on-axis field stop). By design, *b* is kept small to limit the influence of the finite field-of-view of the instrument. To first order, the ILS centered at wavenumber ν_0 is a sinc function ($ILS(\nu-\nu_0) = \sin [2\pi (\nu-\nu_0) X)]/[2\pi (\nu-\nu_0) X)]$). However, for accurate radiometry, it is important to make sure that the FOV is carefully aligned about the central axis of the interferometer and that an effective *b* is determined. Again, we use comparisons with specific regions of calculated atmospheric spectra to refine our nominal values of *b* (based on optical design). The finite field-of-view effect on ILS for the AERI, HIS and NAST instruments is negligible for the longwave band, but can be significant in the shortwave band. Procedures to remove the relatively small effects of ILS wavenumber dependence (ν_0) are routinely applied to the data from AERI, Scanning HIS and NAST.

An example of the spectral scale calibration for the S-HIS from the NASA KWAJEX experiment is shown in Figure 4.

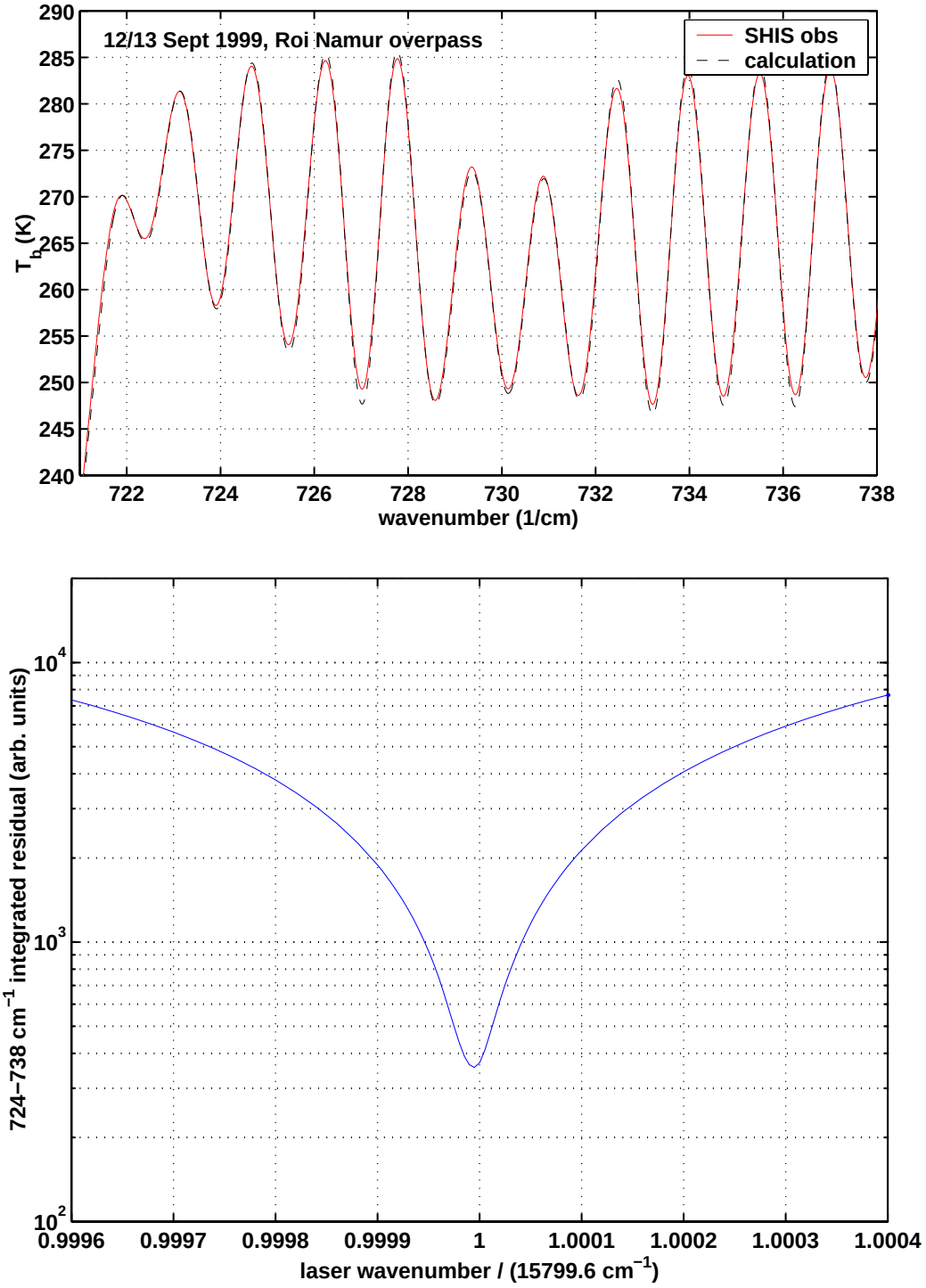

Figure 4. Comparison of observed S-HIS data to a line-by-line calculation for a clear sky overpass of Roi Namur on the September 12/13 flight for several carbon dioxide spectral lines (top panel), and integrated residuals (observed-calculated) for the 724 to 738 cm^{-1} region with the effective S-HIS laser wavenumber (and resulting S-HIS wavenumber scale) perturbed by various amounts ranging from –0.04 to +0.04 percent (bottom panel).

The upper panel shows a comparison of measured and calculated S-HIS spectra for the 722–738 cm^{-1} spectral region from a clear sky flight on 12 September 1999. This spectral region has been chosen for spectral calibration, because of the high accuracy of the measured spectral line parameters of the dominant CO_2 absorption lines in this region. The bottom panel of the figure shows integrated residuals (observed minus calculated) for this spectral region versus the unit-less quantity of the effective laser wavenumber divided by the expected laser wavenumber of 15799.6 cm^{-1}. There is a well defined minimum in this curve, establishing the S-HIS laser wavenumber (and spectral calibration) to better than 1 part in ~ 2×10^5.

3.2 Approach

The major difference between GIFTS and these single-FOV instruments is that each pixel of its imaging detector array has a different wavenumber scale. This effect is a very predictable result of the different angles traversed through the interferometer by the beams focused on each pixel. While the central pixel is nominally the same as the single FOV instruments discussed above, off-axis detectors are irradiated by beams passing through the interferometer at non-zero mean angles. A non-zero mean angle causes the OPD for any given position of the interferometer Michelson mirror to be reduced by the cosine of the off-axis angle.

This OPD scale variation with pixel location is illustrated in Figure 5, which shows a simulated interferogram for the GIFTS longwave band with a uniform scene. For the longwave FPA, the double sided interferogram is sampled at 2048 points. The exact OPD sampling positions, however, vary for each pixel depending on the mean off-axis angle, θ, and the single pixel half-angle, b. The magnified portion of the interferogram illustrated in Figure 5 shows the 0.66 cm region enhanced by the equal spacing of 15 μm CO_2 lines. Three individual OPD points from an on-axis interferogram (0.6637, 0.6654, 0.6671 cm) are also shown for every pixel along the diagonal from the center to a corner pixel of the detector array.

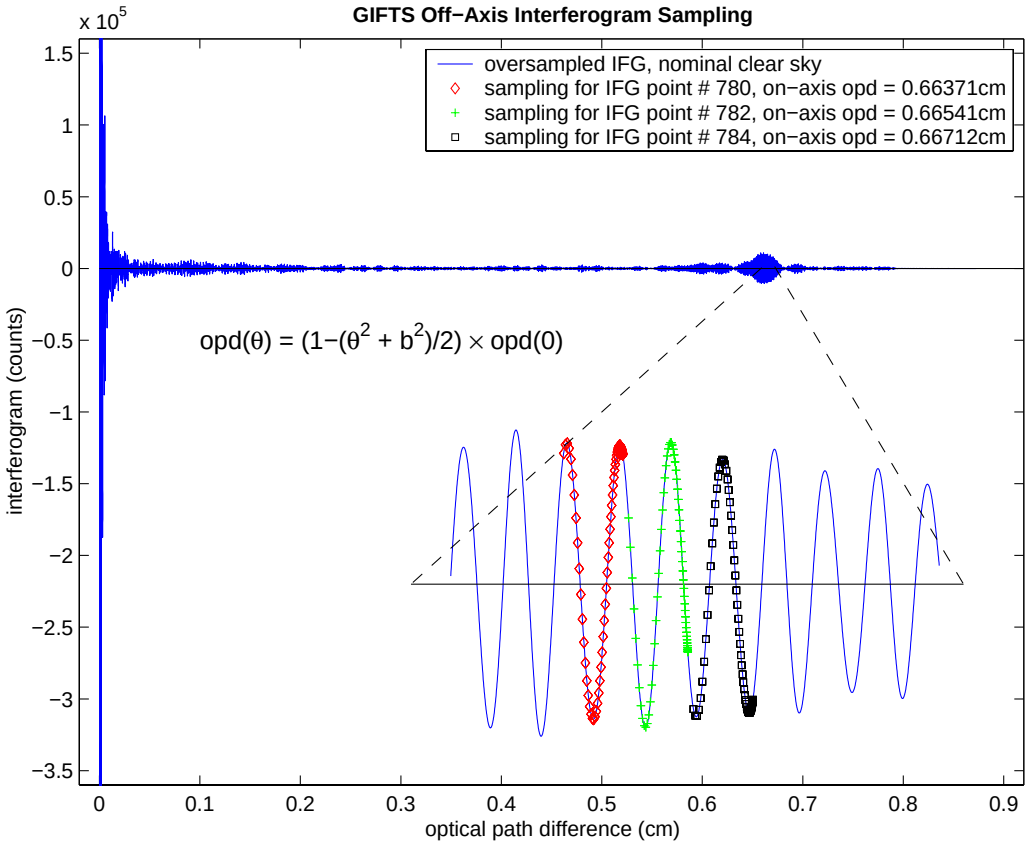

Figure 5. Illustration of the OPD sampling variations due to off-axis beams. The off-axis pixels sample the interferogram at smaller OPDs (compared to the on-axis beams), according to the given equation for OPD(θ). For three different on-axis sample points, the range of off-axis sampling points (from the near-center pixels to the corner pixels of the focal plane array) are shown in the blowup. (See text for more details).

Note that all of the points fall on the same continuous interferogram. For a uniform scene, the only significant difference is a small change in the OPD sampling interval. In other words, the differences are the same as those caused by differences in the effective laser wavenumbers for different instruments, and can be rigorously eliminated by interpolation to a standard scale.

This behavior is realized for the geostationary orbiting GIFTS because of the extremely small range of angles contributing to each individual detector pixel (< 1 mrad in the interferometer). As a result, the variation of ILS across the array is extremely small and can be ignored without introducing significant errors. The ILS is essentially a pure sinc function as illustrated in Figure 6 that also shows the extremely small ILS difference between on-axis and extreme-diagonal pixels.

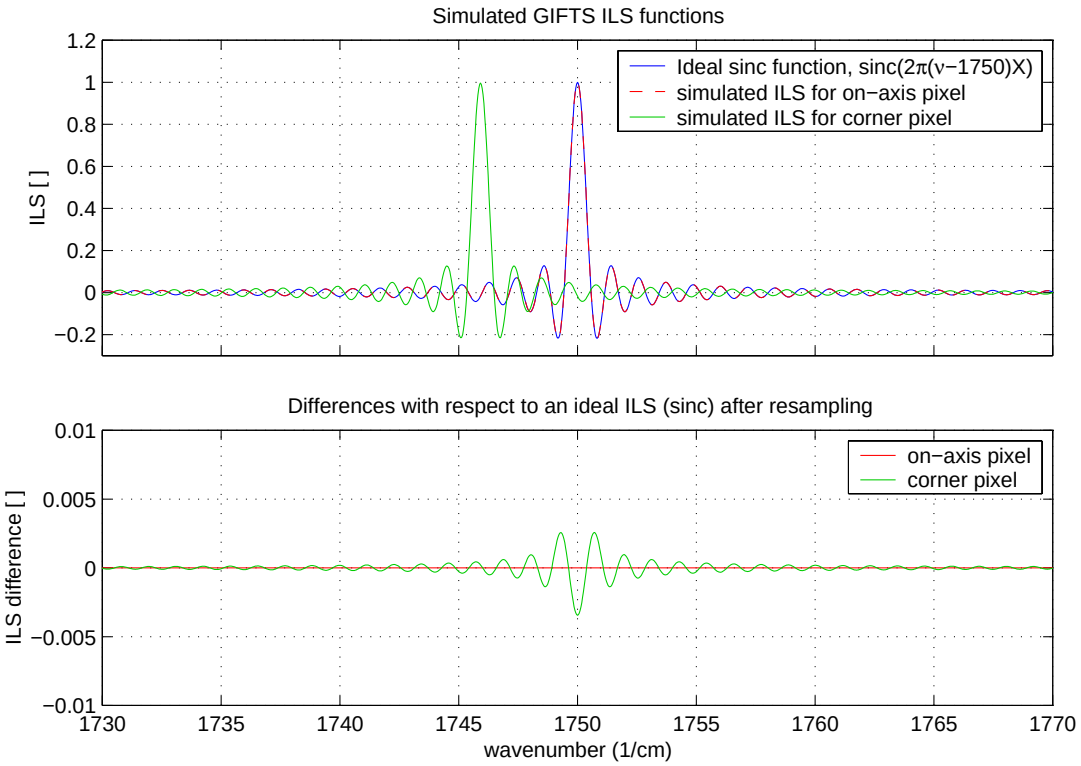

Figure 6. Top panel: comparison of an ideal sinc ILS function centered at 1750 cm^{-1} with simulated GIFTS ILS functions for an on-axis pixel and for a corner pixel (the ideal sinc and the simulated on-axis ILS are indistinguishable in this panel). The shift in the corner pixel ILS is only apparent due to (incorrectly) plotting it on the on-axis sampled wavenumber scale. The bottom panel shows the difference between the corner and on-axis pixel ILS functions from the ideal sinc function after resampling, but without any attempt to correct for the finite detector size effects.

Another way of depicting the small variation of the ILS is to show the small self-apodization in the interferogram domain caused by the finite field-of-view effect. Figure 7 shows that at the extremes of OPD for the GIFTS primary sounding and chemistry mode, the self-apodization variation out to 1750 cm^{-1} is less than 1% over the array. This is very small. In fact, because of the very small angles involved for GIFTS, the deviations from a pure sinc-function ILS are significantly smaller than for the aircraft and ground-based instruments discussed above. Figure 8 shows that the peak brightness temperature effect of ignoring ILS variations is less than 0.15 K for a typical earth scene.

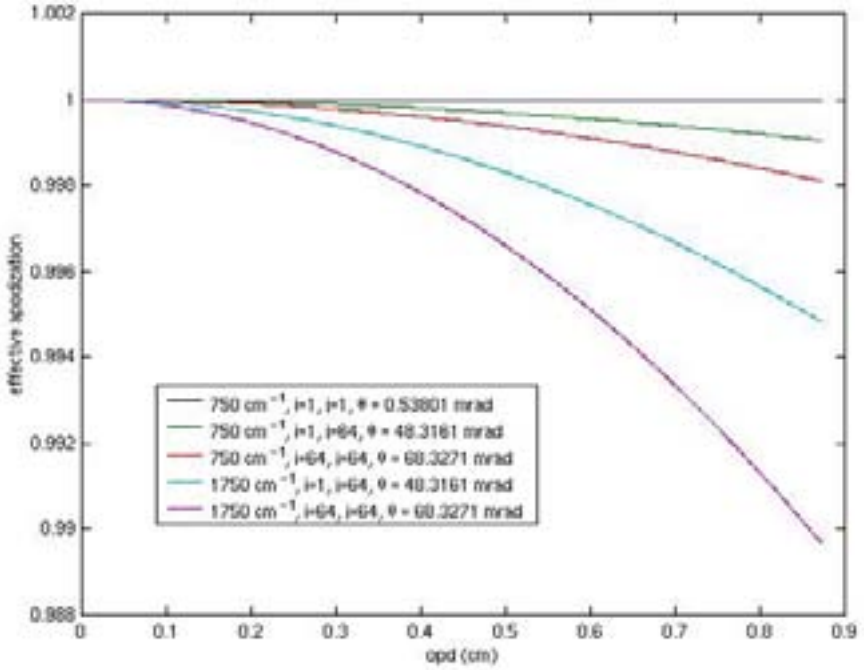

Figure 7. Effective apodization functions due to finite detector size at 750 and 1750 cm^{-1} for various pixel locations. Curves appear in the same order (from top to bottom) as they appear in the legend. In this figure, and in Figure 8, *i* and *j* denote the pixel location within the 128 × 128 FPA, where for example *i*, *j* = (1,1) is near the center of the FPA, and *i*, *j* = (64, 64) is the pixel in the upper right hand corner of the FPA.

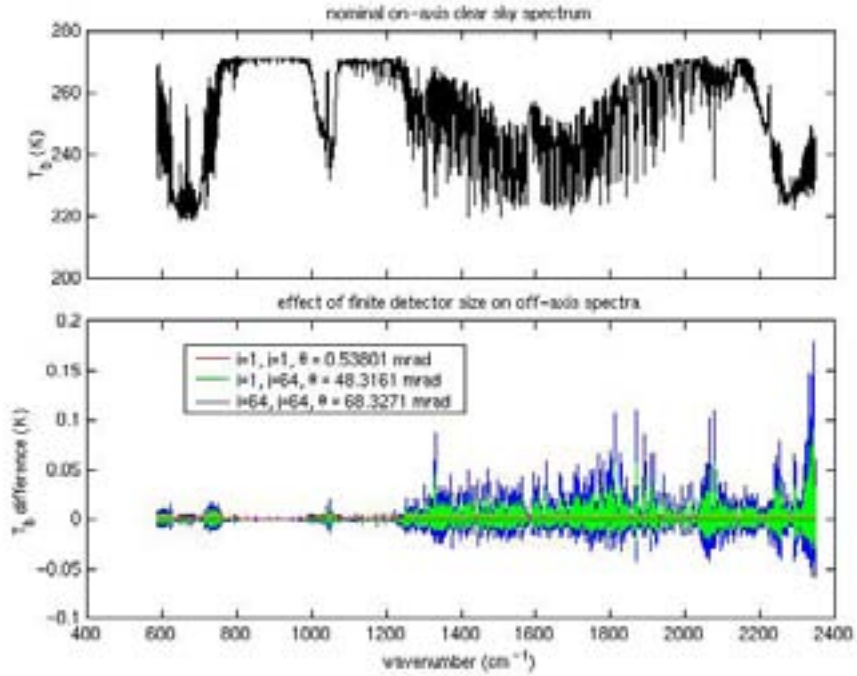

Figure 8. A nominal clear sky spectrum (top panel) and the magnitude of the finite detector size self-apodization effect in brightness temperature (bottom panel) for three FPA pixel locations. In the bottom panel, the *i*, *j* = (1,1) curve is the dark curve near zero, the *i*, *j* = (1,64) has a slightly larger magnitude, and the *i*, *j* = (64, 64) curve has the largest magnitude.

In summary, the imaging Fourier transform spectrometer system used in GIFTS has a well understood ILS and wavenumber scale variation with pixel location. These spectral properties depend on a few well-defined instrument parameters that need to be characterized; namely, the effective wavenumber of the laser used for the detector trigger, and the geometry of the focal plane relative to the interferometer axis. Therefore, spectral calibration can be thought of as very similar to that for a single detector FTS. By observing a localized spectral feature with the central pixel, the effective laser wavenumber can be determined for the central pixel and variations for the other pixels predicted from the known detector and optical geometry. In practice, the spectral scale calibration will be determined for each detector pixel during ground testing with a gas cell before launch. Consistency of these measurements with the known geometry will be verified. Moreover, precise measurements of the ILS will also be obtained from the same gas cell tests.

ACKNOWLEDGEMENTS

A special thanks goes to Brian Osborne who was a major help in assembling and editing this paper. This research was supported by NASA LaRC Contract No. NAS1 00072.

REFERENCES

1. Bingham, G. E., R. J. Huppi, H. E. Revercomb, W. L. Smith, F. W. Harrison,"A Geostationary Imaging Fourier Transform Spectrometer (GIFTS) for hyperspectral atmospheric remote sensing", presented at SPIE's Second International Asia-Pacific Symposium on Remote Sensing of the Atmosphere, Environment, and Space, Sendai, Japan, 9–12 October 2000.
2. Smith, W. L., D. K. Zhou, F. W. Harrison, H. E. Revercomb, A. M. Larar, A. H. Huang, B. Huang, "Hyperspectral remote sensing of atmospheric profiles from satellites and aircraft", presented at SPIE's Second International Asia-Pacific Symposium on Remote Sensing of the Atmosphere, Environment, and Space, Sendai, Japan, 9–12 October 2000.
3. Best, F., H. Revercomb, D. LaPorte, R. Knuteson, and W. Smith, "Accurately Calibrated Airborne and Ground-based Fourier Transform Spectrometers II: HIS and AERI Calibration Techniques, Traceability, and Testing", presented at the Council for Optical Radiation Measurements (CORM) 1997 Annual Meeting, National Institute of Standards and Technology (NIST), Gaithersburg, MD, April 29, 1997.
4. Revercomb, H. E., F. A. Best, D. LaPorte, R. O. Knuteson, W. L. Smith, N. Ciganovich, R. Dedecker, T. Dirkx, R. Garcia, R. Herbsleb, J. Short, "Accurately Calibrated Airborne and Ground-based Fourier Transform Spectrometers I: HIS and AERI Instrument Design, Performance, and Applications for Meteorology and Climate, presented at Council for Optical Radiation Measurements (CORM) 1997 Annual Meeting, National Institute of Standards and Technology (NIST), Gaithersburg, MD, April 29, 1997.
5. Revercomb, H. E., F. A. Best, R. G. Dedecker, T. P. Dirkx, R. A. Herbsleb, R. O. Knuteson, J. F. Short, and W. L. Smith, 1993, "Atmospheric Emitted Radiance Interferometer (AERI) for ARM". In *Fourth Symposium on Global Change Studies*, January 17–22, 1993, Anaheim, California. Published by the American Meteorological Society, Boston, Mass.
6. Goody, R. and R. Haskins, "Calibration of radiances from space", *J. Climate*, **11**, 754–758, 1998.
7. Revercomb, H. E., H. Buijs, H. B. Howell, D.D. LaPorte, W. L. Smith, and L. A. Sromovsky, "Radiometric Calibration of IR Fourier Transform Spectrometers: Solution to a Problem with the High Resolution Interferometer Sounder", *Appl. Opt.*, **27**, 3210–3218, 1988.
8. Revercomb, H. E., L. A. Sromovsky, P. M. Fry, F. A. Best, D. D. LaPorte, Demonstration of imaging Fourier Transform Spectrometer (FTS) performance for planetary and geostationary Earth observing, SPIE's Second International Asia-Pacific Symposium on Remote Sensing of the Atmosphere, Environment, and Space, Sendai, Japan, 9–12 October 2000.
9. Cousins, D., and W. L. Smith, "National Polar-Orbiting Operational Environmental Satellite System (NPOESS) Airborne Sounder Testbed-Interferometer (NAST-I)", *Proceedings of SPIE*, **3127**, 323–331, 1997.
10. Bingham, G. E., D. K. Zhou, B. Y. Bartschi, G. P. Anderson, D. R. Smith, J. H. Chetwynd, and R. M. Nadile, "Cryogenic Infrared Radiance Instrumentation for Shuttle (CIRRIS 1A) Earth limb spectral measurements, calibration, and atmospheric O_3, HNO_3, CFC-12, and CFC-11 profile retrieval", *J. Geophys. Res.*, **102**, D3, 3547–3558, 1997.
11. Menzel, W. P., W. L. Smith, and L. D. Herman, "Visible Infrared Spin-Scan Radiometer Atmospheric Sounder Radiometric Calibration: An inflight evaluation from intercomparisons with HIRS and radiosonde measurements", *Appl. Opt.*, **20**, 3641–3644, 1981.
12. Fowler, J. B., "A Third Generation Water Bath Based Blackbody Source", *J. Res. Nat. Inst. Stand. Technol.*, **100**, 591–599, 1995.
13. Kannenberg, R., "IR Instrument Comparison Workshop at the Rosenstiel School of Marine and Atmospheric Science (RSMAS)", *The Earth Observer*, EOS Project Science Office, Vol 10, No. 3, May/June 1998 (http://eospso.gsfc.nasa.gov/earth_observ.html).